Published in final edited form as:

IEEE Trans Med Imaging. 2009 May ; 28(5): 710–719. doi:10.1109/TMI.2008.2010441.

A Computational Geometry Approach to Automated Pulmonary Fissure Segmentation in CT Examinations

Jiantao Pu, **Joseph K Leader**, **Bin Zheng**, **Friedrich Knollmann**, **Carl Fuhrman**, **Frank C Sciurba**, and **David Gur**

Imaging Research Center, Department of Radiology, University of Pittsburgh, 3362 Fifth Avenue, Pittsburgh, PA 15213

Abstract

Identification of pulmonary fissures, which form the boundaries between the lobes in the lungs, may be useful during clinical interpretation of CT examinations to assess the early presence and characterization of manifestation of several lung diseases. Motivated by the unique nature of the surface shape of pulmonary fissures in three-dimensional space, we developed a new automated scheme using computational geometry methods to detect and segment fissures depicted on CT images. After a geometric modeling of the lung volume using the Marching Cube Algorithm, Laplacian smoothing is applied iteratively to enhance pulmonary fissures by depressing non-fissure structures while smoothing the surfaces of lung fissures. Next, an Extended Gaussian Image based procedure is used to locate the fissures in a statistical manner that approximates the fissures using a set of plane “patches.” This approach has several advantages such as independence of anatomic knowledge of the lung structure except the surface shape of fissures, limited sensitivity to other lung structures, and ease of implementation. The scheme performance was evaluated by two experienced thoracic radiologists using a set of 100 images (slices) randomly selected from 10 screening CT examinations. In this preliminary evaluation 98.7% and 94.9% of scheme segmented fissure voxels are within 2 mm of the fissures marked independently by two radiologists in the testing image dataset. Using the scheme detected fissures as reference, 89.4% and 90.1% of manually marked fissure points have distance ≤ 2 mm to the reference suggesting a possible under-segmentation of the scheme. The case-based RMS (root-mean-square) distances (“errors”) between our scheme and the radiologist ranged from 1.48±0.92 to 2.04±3.88 mm. The discrepancy of fissure detection results between the automated scheme and either radiologist is smaller in this dataset than the inter-reader variability.

Keywords

Pulmonary fissure; Segmentation; Computer-aided detection; Shape analysis; Extended Gaussian Image (EGI)

I. INTRODUCTION

Pulmonary disease is reported as the third leading cause of death in the United States [1]. Thin-section, multi-detector, x-ray computed tomography (CT) of the chest has been widely used to detect and diagnose pulmonary disease. Pulmonary fissure integrity and the characteristics of tissue adjacent to the fissure may play an important role in identifying and characterizing chronic obstructive pulmonary disease (COPD) and interstitial lung disease

---

Corresponding Author: Jiantao Pu, Ph.D., Department of Radiology, University of Pittsburgh, 3362 Fifth Avenue, Pittsburgh, PA 15213, Tel: (412)-641-2571, Fax: (412)-641-2582, puj@upmc.edu.

(ILD) as well as the presence of early disease in general [2]. A robust detection of pulmonary fissures could provide a basis for accurate lobe segmentation that may help facilitate pre-operative planning and post-operative assessment in the clinical practice [3, 4]. Pulmonary fissures could also be used as landmarks for intra-patient registration during sequential imaging assessments [5]. Therefore, the development of a robust, automated fissure detection tool may be beneficial to quantitative lung image analysis that can be incorporated into other computer-aided detection and diagnosis (CAD) schemes for different clinical applications.

The fissures that divide the lung into lobes consist of double layers of infolded invaginations of the visceral pleura. Typically fissures are approximately 1 to 3 mm thick [6]. In general, the fissures are depicted as relatively thick bands that are somewhat denser than surrounding lung tissue on low through-plane resolution CT images and as relatively narrow lines on thin-section images with high through-plane resolution. Unfortunately, fissures are typically depicted with wide variation in pixel value distributions and with often blurred (fuzzy) boundaries, which make it difficult to differentiate from other lung regions. Therefore, it is virtually impossible in most cases to use a simple threshold to segment the fissure from its surrounding structures. In addition, the presence of other surrounding lung structures (i.e., vessels and airways), disease patterns (i.e., tumors, atelectasis, or emphysematous changes), and CT image noise makes automated detection of the fissures a challenging task.

A large number of segmentation methods (e.g., airway, vessel and lung segmentations) [5–15] related to volumetric pulmonary CT imaging have been developed, however, a few of these have attempted to address pulmonary fissure or lobe detection and segmentation. Most of these methods are based on exploiting knowledge of the pulmonary anatomy and are implemented in either two- or three-dimensional image space. The first type of anatomy knowledge used in developing automated schemes is that pulmonary fissures look like curved lines on two-dimensional CT images and can be continuously traced through neighboring slices. The previously developed schemes using this knowledge included the curve-growing strategy [16, 17], the Vanderbrug linear feature detector [18], and the Gaussian and mean curvature analysis approach [19]. Despite their simplicity, these schemes often need the initial growth seed (starting point) delineated manually on the CT images, and it is difficult to identify two-dimensional disjointed fragments that belong to the same fissures.

The knowledge that in general no large vessels should be depicted near the fissures has also been explored. Schemes using this type of information include the interactive three-dimensional watershed algorithm [20], the edge (or plane) detection based lobe estimation method [21], and the blood vessel classification based approach [22]. The limitations and difficulties of these schemes include (1) heavy dependence on pulmonary vessel segmentation and voxel classification, which is often a complex process and sensitive to the selected threshold [20], (2) inaccuracy in applying Hough transform to detect curved surfaces [21], and (3) inability of detecting abnormal lung structures (e.g., in cases with accessory fissures or more than 5 lobes) [22].

In addition to the above mentioned methods that took advantages of the local anatomy knowledge, Zhang et al. [23–25] developed a lobe segmentation method based on a global pulmonary atlas encoded with gray level information and anatomic shape characteristics. First, a fuzzy reasoning scheme was used to construct an anatomic atlas using 16 pre-segmented volumetric CT scans. Then, after enhancing the contrast of the original CT images using a ridge operator, a graph search engine was used to detect the fissures with the help of the anatomic atlas and specific shape constraints. As a complex process, the performance of this approach relies on a number of factors such as the quality of pulmonary atlas, graph search engine and the pre-defined shape constraints. Recently, van Rikxoort et al. [26] proposed using a pattern recognition procedure based on training data and a “supervised filter” to enhance pulmonary fissures.

Computerized schemes developed to date consider primarily global similarity of lung anatomy in all patients and often ignore individual variability [27]. Therefore, we developed and tested a new automated pulmonary fissure detection and segmentation scheme. The motivation for our approach is to reduce dependence on anatomical knowledge that may have large variability among imaged individuals and to minimize the possible impact of unrelated lung tissue structures (i.e., vessels, airways and tumors) on the performance of the scheme. For this purpose, our scheme applies a computational geometry methodology combined with statistical analysis to detect regions with three-dimensional surface shape assumed to be part of the fissures depicted on lung CT examinations. The geometric representation (model) of the pulmonary fissures obtained by this approach is expected to provide an intuitive representation of fissures and their completeness (or lack thereof). A detailed description of the proposed scheme and preliminary test results when applied to a limited dataset are presented in this article.

II. MATERIALS AND METHOD

A. Clinical Dataset

To develop and test the proposed automated fissure detection and segmentation scheme, we randomly selected a dataset of 10 chest CT examinations acquired from a COPD (chronic obstructive pulmonary disease) screening cohort at the University of Pittsburgh Medical Center. All participants had a relatively low level of airflow obstruction measured or were identified as visually depicting emphysema on their CT examinations. An experienced chest CT radiologist visually reviewed and rated the CT examinations for the presence (or absence) of emphysema as negative, trace, mild, moderate, and/or severe. The presence (or absence) of emphysema was rated as “negative” in six subjects and “trace” in the remaining four subjects. Pulmonary function tests (PFT) were performed using body plethysmography (Vmax 229 AutoBox, SensorMedics, Yoba Linda, CA). The percent predicted of forced expiratory volume in one second (FEV_1%) and forced vital capacity (FVC%) were computed for each participant with mean values across the 10 subjects of 93.9 (±20.8) and 95.1 (±18.2), respectively.

The CT examinations used in this study had been performed under an IRB approved protocol using a LightSpeed VCT 64-detector scanner (GE Healthcare, Waukesha, WI) with subjects holding their breath at end inspiration. CT data were acquired using a helical technique at a pitch of 0.969, 120 kVp, 0.4 sec gantry rotation, and 250 mA (or 100 mAs). The detector configuration was 32 × 0.625 mm. CT images were reconstructed to encompass the entire lung field using the GE “bone” kernel at 0.625 mm section thickness and 0.625 mm interval. The CT images were represented using a 512 × 512 pixel matrix with a patient size dependent pixel dimension ranging from 0.549 to 0.738 mm.

B. Overview of the Automated Scheme

The relatively fuzzy visual appearance (i.e. low conspicuity) of fissures and other structures depicted on CT images is one of the primary obstacles for accurate automatic segmentation. In order to overcome this difficulty, we propose an automated scheme based on computational geometry approaches, which exploits the fact that pulmonary fissures are depicted on CT images as three-dimensional surfaces with thickness of but a few millimeters. The proposed approach contains essentially four steps (Fig. 1) including (1) lung segmentation, (2) lung thresholding, (3) initial fissure detection, and (4) fissure extension.

C. Lung Segmentation and Thresholding

The first step of our scheme is to segment lung area depicted on CT images. The purpose of this step is to limit the searching space during the fissure detection, thereby improving computational efficiency and eliminating the possibility of erroneous fissure detection outside the lung. Unlike other detection tasks such as lung nodule detection [28–32], the smoothness of the lung boundary has little effect on fissure detection. Therefore, we used an established and computationally efficient threshold-based region-filling strategy to segment the lung area depicted on CT images (Fig. 2(a)–(b)). The threshold is determined automatically as described by Armato et al. [32].

The next step of our scheme applies a threshold method to identify initially suspicious pixels within the segmented lung area, which may be associated with the fissures. Due to their fuzzy appearance, lower conspicuity, and large variation in pixel intensity, pulmonary fissures are difficult to segment from their surrounding structures using a fixed threshold. Based on our observation involving 20 randomly selected chest CT examinations, we found that the intensity (voxel value) of fissures ranged mainly between −800 HU (Hounsfield Unit) and −400 HU. Thus, a heuristically determined threshold band was implemented in our scheme and applied to the segmented lung volume. All voxels with digital value between −800 HU and −400 HU remain and all other voxels are deleted (Fig. 2 (c)). This step substantially reduces the number of voxels to be searched and eliminates the majority of non-fissure linear structure (e.g., vessels), while maintaining high sensitivity in detecting fissure voxels. This process cannot assure complete reservation of all fissure voxels but it improves computational efficiency in the next fissure modeling and detection procedure.

D. Initial Fissure Detection

The thresholded image contains fissures, other lung tissue structures and isolated voxels representing “noise” (Fig. 2 (c)). A traditional image smoothing operation (e.g., a Gaussian filter) cannot be applied to the images because the fissures may be “smoothed out” together with image “noise”. To overcome this difficulty, we applied a statistical approach to extract the pulmonary fissures in three-dimensional geometric space. This approach can distinguish between fissure surface (curved plane) and isolated small regions with random normal vectors (orientations). Following is the main idea of our approach to detect and extract fissures.

(1) Lung Sub-volume Modeling and Laplacian Smoothing—In our study, we use the widely used Marching Cube Algorithm (MCA) [33] to construct a triangle based mesh from a three-dimensional scalar field (or voxels). Fig. 3 shows how the method is applied to a sub-volume (i.e., a small cubic region) whose center was positioned on the fissure with a size of 50×50×50 mm^3. Fig. 3(a) shows the initial fissure model generated by MCA when applied to the thresholded images (within −800 HU ≤ threshold band ≤ −400 HU) and is generally quite noisy. To better differentiate the fissure from other tissues and isolated voxels, we use the Laplacian smoothing method [34] that adjusts the location of each mesh vertex to the geometric center of its neighboring triangles without modifying the topology of the mesh. Assuming a vertex P_i is surrounded by n triangles, its adjusted location P_i' after Laplacian smoothing is:

$$P_i' = \frac{\sum_{k=1}^{n} a_k C_k}{\sum_{k=1}^{n} a_k} \quad (1)$$

where a_k is the area of the k^{th} neighboring triangle, and C_k is the mass center of that triangle, which is the average of the three vertices. A smoothing operation requires sweeping through all mesh vertices. Obviously, the computational cost is linear to the number of vertices. The Laplacian smoothing has two properties that fit our requirements in developing this automated scheme for lung fissure detection and segmentation [35, 36]: (a) *The smoothing operation will shrink the size of the object represented in the form of a triangle mesh*; (b) *Given a vertex of a triangle mesh, the normals of the neighboring triangles tend to be similar after the Laplacian smoothing*. The first property reduces high-frequency components (e.g., the small clustered regions formed by other non-fissure lung structures and remaining isolated voxels), but requires a larger number of iterations for lower frequency components (e.g., fissures); while the second property tends to flatten the surface, which means that the normals of the neighboring triangles tend to be similar.

Due to the discrete distribution and small size, the surfaces formed by unrelated voxels are primarily degenerated into isolated points or substantially smaller regions after repeated Laplacian smoothing operations. The repeated Laplacian smoothing operations also flatten the surface of the remaining planes (i.e., fissure plane) by correcting the discontinuity of the surface normal vectors. Thus, repeatedly applying the Laplacian smoothing operations can gradually eliminate isolated voxels or small regions, while the fissure surfaces remain and become smoother (Fig. 3(b)–(c)).

(2) Fissure Normal Computation based Extended Gaussian Image (EGI)—To simplify the fissure detection procedure, we use a set of plane patches to approximate the fissure surfaces in three-dimensional space. If the size of the sub-volume is small enough, the shape of the contained fissure patch can then be approximated by a plane patch. As a result of the Laplacian smoothing operations, the normal vectors of the triangles that form the fissure patch tend to be similar. Therefore, the fissure detection task is transformed into the extraction of these plane patches. To take advantage of the fact that these planes usually have similar normal vectors at each point, we use an Extended Gaussian Image (EGI) approach [37] as the representation basis for fissure detection. EGI is a statistical approach to determine the attitude of an object in space by finding the normal vector with the largest projected area. The surface normal vector of an object is mapped onto a unit sphere termed the Gaussian sphere and a weight is assigned to each point on the Gaussian sphere equal to the area of the surface having a given normal. The resulted mapping is called a Gaussian image of the object. The EGI is not affected by the translation of an object. Rotation of an object leads to an equal rotation of the EGI. The detailed steps of constructing the EGI for an object have been explained in details by Horn [37].

After the Laplacian smoothing, the smoothed model is represented in the form of EGI. The normal vector of the plane where a fissure patch is located will have the largest value in the EGI. In contrast, the randomness of other structures will lead to a random normal distribution in EGI. Therefore, the largest value in the EGI is represented primarily by the normal vector of the fissure in the sub-volume (Fig. 4(a)).

(3) Fissure Extraction by Area Histogram Analysis—Given the normal vector n of a fissure patch, we need to find a point in order to uniquely determine the plane on which the fissure patch is located. To detect this plane, a geometric transformation is first performed to rotate and align the normal vector with the z-axis that is perpendicular to the CT image slices (Fig. 4(b)). Second, a histogram is constructed by summarizing the areas of the triangles according to the z coordinates values of their centroids (Fig. 4(c)). The bin size of this histogram is simply set as 1 mm. Since majority of the triangles are located in the plane on which the fissure patch is located, the maximum value of the histogram corresponds to the location of the fissure patch along the z-axis. Thereafter, we project the fissure model onto this plane and determine the axis-aligned bounding box (AABB) of the projected points. This two-dimensional bounding box is regarded as the fissure patch in the specific sub-volume.

To implement our concept of fissure detection, as we explained in the example using a sub-volume (Fig. 3 and Fig. 4), we first used an axis-aligned bounding box (AABB) to establish a volumetric grid system in a CT examination as shown in Fig. 5(a), where each cell has a size of 5×5×5 mm^3. Centered on each vertex of the grid system is a 15×15×15 mm^3 sub-volume of CT data that is extracted and processed using the MCA for modeling purposes. Because the smoothed lung boundary surface may be classified as fissure surface (as shown in Fig. 5(b) and (c)), our scheme only extracts sub-volumes that are completely located inside the lung volume. The sub-volume is larger than the cell of the grid system; hence it creates overlap between neighboring sub-volumes, which is designed to detect fissures as much as possible for later extension purpose. The underlying principle for sub-volume size determination is that a partial fissure within a sub-volume should approximate a plane.

Considering the fact that the fissures have a relatively higher intensity as compared to their surrounding structures and their intensity levels vary in different lung sections, we proposed and tested an adaptive strategy for threshold selection that was determined by the average intensity of the voxels within a specific sub-volume. Then, after applying MCA with Laplacian smoothing operation, EGI mapping, and histogram analysis, the scheme detects the largest plane (area) projected along the normal direction inside each sub-volume. A strict classification rule was implemented to classify whether the largest plane patch detected in a sub-volume is part of a fissure. The rule requires that the area of the triangles forming a detected "fissure patch" (i.e., the largest value of the histogram in Fig. 4(c)) must be larger than 125 mm^2, which is approximately half of the intersection area between the fissure and the sub-volume when two sides of the fissure surface are considered. After sweeping all volume grids and detecting initial fissure patches, the scheme transforms the detected plane patches from the geometric space to the original CT image space. The voxels, which have intensity larger than −800 HU and are within a specific distance (e.g., 2 mm) to the plane patches, are marked as fissure with the consideration of the thickness of fissures. As an example, the initial fissure detection result of a CT slice shown in Fig. 2(a) is marked in Fig. 6(a).

E. Fissure Extension

Because the initially detected set of fissure plane patches may contain possible discontinuities and/or missing sections due to the strict classification rule in the above initial fissure detection used to check the existence of the fissures in a sub-volume, the fourth step of the scheme aims to build a complete fissure surface by extending detected fissure patches. The scheme sweeps the CT data and searches for voxels belonging to previously detected fissure patches. Once a target is identified, the scheme creates a new sub-volume (15×15×15 mm^3) centered at this voxel. Since this sub-volume contains a partial fissure that had already been detected and may contain a partial fissure that is not detected yet, the scheme will extend the fissures by using the normal vector of the already detected fissure patch to find the whole fissure patch in the sub-volume. Unlike the initial fissure detection procedure, this extension step does not consider the classification rule used to check the existence of the fissures in a sub-volume because there must be a fissure patch within the sub-volume that is centered at a voxel identified belonging to a fissure. The repeatedly detected voxels (for the second time) in the sub-volume are marked as “visited” and these are not repeatedly used as growth seeds in the fissure extension operation. The voxel in the extended plane must have a digital value larger than −800 HU to avoid the misclassification of normal lung tissue area such as parenchyma as fissures. By iteratively repeating the above scanning and extension procedure, the scheme can gradually recover the missing section of fissures. This fissure extension process is terminated when no additional voxels can be identified as fissures, namely no fissure area expansion occurs during the iteration. As an example, we show the initial fissure detection result in Fig. 6(a) and the extended fissure lines in Fig. 6(b).

F. Performance Assessment

To evaluate the performance of our computerized scheme 100 CT images were selected from the 10 CT examinations (10 per examination). These were distributed equally across the lung area with all three fissures (i.e., right oblique, right horizontal, and left oblique) depicted in one or more images. Two experienced thoracic radiologists independently reviewed and manually traced the fissures depicted on the 100 CT images. We conducted two experiments. First, the radiologists were presented the 100 images with the automated fissure detection results as an overlay and instructed to modify (add or delete pixels) the fissure detection results using the computer mouse. During this process the radiologists could toggle the computerized results off and on in real time. Next, the radiologists were presented 10 images randomly selected, one from each examination without the availability of the automated fissure detection results, and they were asked to manually trace (plot) the complete fissure using the computer mouse. We use the manual fissure detection results of the two radiologists to assess the agreement or discrepancy between two radiologists (inter-reader variability) as well as between each radiologist and our computerized scheme. We assessed the discrepancy, if any, in detecting fissures with and without viewing the automatically detected fissures by the scheme.

The cumulative error distance distribution (CEDD) was used as a primary measure of discrepancy between paired fissure detection results as determined (marked) by the automated CAD scheme and/or the radiologists. The CEDD is computed as the cumulative percentage of the shortest distance between each of the points located in the testing set of fissures to any point located in the reference set. This measure not only indicates the fraction of fissures fitted between two point sets within a specific error but also provides an assessment of over- and under-segmentation. First, we used fissures traced and marked by radiologists as the reference and computed CEDD for the scheme segmented fissures. When the shortest distance from a point on the detected fissures to the reference created by radiologists is larger than a specific value (e.g., 4 mm), it signifies the over-segmentation of our computerized scheme (i.e., misclassifying some small regions or planes as fissures). We also used fissures segmented by our scheme as the reference and computed CEDD for the fissures manually marked by the radiologists. Similar to the above mentioned idea of over-segmentation, this measure enables an assessment of under-segmentation of the computerized scheme. Root-Mean-Square (RMS) distances (“errors”) of fissure detection results between the computerized scheme and each of the radiologists and between the two radiologists were computed. To evaluate the robustness and generalizability of the results to this type of a dataset we bootstrapped the results on cases and images with replacement separately (1000 samples) and computed 95% confidence intervals.

III. RESULTS

Examples of our automated fissure segmentation results are shown in Fig. 7 and Fig. 8, respectively. In the two-dimensional display, the segmented results are shown from three different sections including the axial, coronal, and sagittal sections (Fig. 7). It shows that our scheme captures the thickness of the fissures in addition to their locations. Since our method detects all regions with surface shape as fissures when the size of the identified region is larger than a predetermined threshold, the accessory fissures (Fig. 8(b)) and non-fissure surface shape regions may also be detected and segmented (as indicated by the arrow in Fig. 7(c)).

In the three-dimensional display, the segmented fissures are modeled and visualized in a geometric form modeled by the MCA. It preserves the completeness of the fissures and also a few misclassified patches. For example, the small patches shown in Fig. 8(c) correspond to the region indicated by the arrow in Fig. 7(c)). These small patches could be deleted possibly by a size based rule because they are frequently substantially smaller than actual fissures. However, in this study, the detected accessory fissures and other small non-fissure surface shape regions remain and are computed in the CEDD assessment of fissures since they had been detected and/or marked by either the scheme or the radiologists or both.

Fig. 9 shows three sets of cumulative error distance distribution (CEDD) curves of the completed differences (“errors”) between the results of the computerized scheme and each of the radiologists as well as the differences between the two radiologists (representing an inter-reader variability). In the three sets of CEDD curves, different comparison references are used. Specifically, the fissures marked by radiologist #1, marked by radiologist #2, detected and segmented by the computerized scheme, represent the references used in Fig. 9 (a), (b), and (c), respectively. Each curve set includes four CEDD curves. Two curves represent the assessment results when detecting fissures depicted on the 100 CT images in which the radiologist marked the fissures with knowledge of the scheme detected results (experiment one). The other two curves represent the detection discrepancy over the 10 CT images in which the radiologist traced fissures without knowing the results of our scheme (experiment two). In experiment one, a relatively large inter-reader variability between the two radiologists was found. In this dataset Radiologist #1 plotted a larger number of and also longer fissure curves than radiologist #2. Thus, when using the fissures marked by radiologist #2 as the reference, the CEDD curve (R1 – R2) rises slower (Fig. 9(b)) than the CEDD curve (R2 – R1) using the fissures marked by radiologist #1 as the reference (Fig. 9(a)). The large difference between two curves representing discrepancy between our scheme and radiologist #1 (C – R1 in Fig. 9(a) and R1 - C in Fig. 9(c)) shows that our scheme missed more fissure sections (points) marked by radiologist #1 (under-segmentation). However, in experiment two, the inter-reader variability of two radiologists is reduced. As a result, the fissure segmentation discrepancy between our scheme and either radiologist becomes smaller and more consistent.

Table 1 summarizes the Root-Mean-Square (RMS) distances (“errors”) of fissure detection results between the computerized scheme and each of the radiologists as well as between the two radiologists. Depending on the “reference” being used (as shown in Fig. 9), the RMS distances range from 1.48±0.92 to 2.04±3.88 mm for the automated scheme versus the radiologists and these are smaller than the RMS distances between the two radiologists (3.34±4.98 and 2.64±2.76 mm). We note that cases #7 and #9 have much larger RMS distances than the other eight cases which are also seen as large CEDD differences in Fig. 9. These two cases are partially affected by the small planes that are detected and misclassified as fissure planes by the scheme (e.g., Fig. 7(c) and Fig. 8 (c)). However, the primary reason for the difference stem from the detection of accessory fissures by the CAD scheme in these two cases (e.g., Fig. 8(b)). These accessory fissures were ignored (completely un-marked) by Radiologist #1 in two cases and by Radiologist #2 in one case. The larger computed distances stem from the points located and detected on the accessory fissures to the closest reference points on fissures actually marked by the radiologists. The case based 95%

confidence intervals for the RMS distance values between the radiologists and the computerized results as estimated from the bootstrapping procedure are [0.197, 4.533] mm and [0.833, 3.879] mm for Radiologist #1 and #2, respectively. The corresponding image based 95% confidence intervals were [0.202, 1.862] mm and [0.442, 1.892] mm. When the cases in which accessory fissures were not marked by either of the radiologists were excluded from the analysis (cases # 7 and #9) the case based 95% confidence intervals decreased to [0.135, 0.367] mm and [0.667, 1.637] mm, respectively. The corresponding image based confidence intervals decreased to [0.141, 0.282] mm and [0.358, 0.580] mm.

Table 2 summarizes the agreement rate between our scheme and the two radiologists when using 2 mm and 3 mm as the threshold for the smallest distance difference between two sets of segmented fissure data. The larger the number, the higher the rate of agreement is. The agreement rates between two compared fissures vary depending on which one is used as the referenced fissure. For example, when using fissures marked by radiologist #1 as a reference in experiment one, the distances of 98.7% of fissure points detected by the scheme (CAD → R1) are less than 2 mm away from the radiologists' marked fissures; while when using automated segmented fissure as a reference, only 89.4% of fissure points marked by radiologist #1 (R1 → CAD) have distance smaller than 2 mm to reference fissure. The table also indicates the under-segmentation of our scheme as compared to the fissure marked by this radiologist. In general, the data summarized in this table also show that the agreement in fissure segmentation results between our scheme and either of the radiologists is smaller than the inter-reader variability between the two radiologists themselves.

IV. DISCUSSION

In this study, we developed and tested a new automated scheme for detecting and segmenting pulmonary fissures. Our scheme has a number of unique characteristics and advantages. First, since our scheme only focuses on searching for and detecting all surface shape structures depicted in the CT examination, it reduces the dependence on anatomy knowledge or other underlying assumptions that are often affected by large variation among individuals. This characteristic allows our scheme to relatively easily detect accessory fissures (e.g., Fig. 8(b)). Second, other lung structures and/or isolated clusters of voxels generated by different image processing or filtering algorithms have little impact on the detection performance since the underlying concept takes into account the fact that pulmonary fissures are relatively large and are connected three-dimensional surfaces with thicknesses of a few millimeters. Third, we applied a unique iterative Laplacian smoothing operation that enables an incremental decrease of small regions generated by other lung structures into isolated points or much smaller regions, followed by an eventual elimination. In addition, the approach smoothes the detected fissure plane by increasing the similarity of the average normal vectors. Fourth, as a result of using the EGI computed normal vector histogram to classify fissure plane patches and other non-fissure structures, our scheme is relatively insensitive to voxel intensity variation across different lung areas. Fifth, since the detection procedure is performed in a geometric space, the detected fissures are readily represented in the form of a three-dimensional model and can be used to provide an intuitive representation of fissures and their completeness (or lack thereof). For a typical CT dataset consisting of approximately 450 image slices (with a slice thickness 0.625 mm), our scheme takes approximately 9 minutes to detect the fissures when using a desktop PC computer installed with an AMD Athlon™ 64×2 Dual 2.11GHz central processor and 2GB RAM.

The primary limitation of our scheme actually arises from its lack of dependence on known anatomy characteristics. For lung CT images depicting disease some plane-like tissue structures (e.g., interstitial disease) may be incorrectly detected as fissures due to their possible surface shape appearance in three-dimensional space. Although these non-fissure planes may be ultimately differentiated from fissures because these regions often generate smaller plane patches than actual fissure planes (as shown in Fig. 8(c)), this approach could discard small fissure sections in cases with severe lung disease. Developing robust methods to classify between incomplete small fissure sections and other non-fissure regions is the topic of our current investigation.

The lack of a verified “ground-truth” also presents a problem in term of absolute performance assessment [38–40]. In this preliminary study, we evaluated the performance and reliability of our scheme on a relative scale as compared with the markings of two experienced radiologists. We recognize that the assessments in this project are not absolute and do not use the “ground-truth” pulmonary fissures. However, when comparing our scheme to the reference, our scheme achieved a reasonably promising fissure detection and segmentation results. The RMS distance differences between our computerized fissure segmentation and either of the radiologists are smaller than the differences between the two radiologists themselves (Fig. 9 and Table 1). The results reported here can not be directly compared with other studies due to differences in sample selection, data acquisition and data processing protocols. However, we note that our results are in the range of other reported studies in which the RMS distances ranged from 0.75±0.68 to 2.15±1.59 mm in a set of 10 testing CT cases [16] and 1.67±0.53 mm and 2.30±0.76 mm when comparing a set of selected CT images from 12 TLC (total lung capacity) scans and 10 FRC (functional residual capacity) scans, respectively [25]. Our results are better than these previously reported results when the accessory fissures ignored (completely not marked) by the either of the radiologists are excluded from the analyses.

Interestingly, large intra-reader variability in manually marked fissures has also been found during these experiments (“with” and “without” viewing the fissure detection results of the computerized scheme during the experiment). The larger inter-reader variability when the results of our scheme were available to the radiologists (as shown in Fig. 9) suggests that the two observers considered or “accepted” our automated fissure segmentation results differently. We note that this is a preliminary study involving only two radiologists and small number of images. Thus, further studies are needed to (1) investigate the impact of viewing automated fissure segmentation results on radiologists’ performance in fissure detection and (2) identify optimal approach to evaluate the performance and reliability of automated fissure detection and segmentation schemes.

Despite their close relationship, lung fissure and lobe detection and segmentation are different tasks. Lung fissures do not always represent the boundary between lobes and the lobe segmentation does not mean a direct segmentation of fissures because there is always potential of incompleteness of fissures [38]. The examples shown in Fig. 8 demonstrate the “raggedness” of the fissures detected and segmented by our scheme primarily due misclassification of non-fissure voxels (in particular along the fissure boundary) and incomplete fissure representation or “missing” fissure voxels. Although this study only focused on fissure detection and segmentation, our unique approach has the potential to enable the detection, classification and quantification of the completeness (or leakage) of fissure surfaces depicted on CT images. This could be important for evaluating the relationship between fissure incompleteness and functional severity of different lung disease. Correct classification and recognition of the different fissures and their configurations is an important issue that needs to be addressed if one is interested in extending this approach to lobe segmentation. For this purpose, recognition of the major, minor, and accessory fissures is required and one could apply available shape analysis approaches [41–43], however, this task is beyond the scope of this work.

We recognize that this is a very preliminary study in which a relatively small dataset with 10 CT examinations of fairly normal lung subjects was selected and used to test the new computerized scheme for lung fissure detection and segmentation. We also realize that these examinations had been acquired at high in-plane and through-plane resolution and reconstructed with some edge enhancement (GE "bone" reconstruction kernel) which is not always the case in the clinic. However, this approach has to be demonstrated first under somewhat "favorable" conditions before it is extended to other scanning protocols. Although the feasibility of our new approaches and the scheme has been demonstrated, the robustness of the scheme needs to be further tested using a large and diverse database including some abnormal or diseased lung CT examinations.

V. CONCLUSION

We developed a new automated pulmonary fissure detection and segmentation scheme with virtually no dependence on prior knowledge of lung anatomy except the surface shape of fissures. The anatomy knowledge dependence could add complexity due to the large variability in lung anatomy among individuals. The scheme uses a computational geometry based approach, including the MCA, Laplacian smoothing, and EGI to achieve high detection sensitivity of fissure plane patches and eliminate other non-fissure related patches. The performance of this scheme was tested in relationship to that of two radiologists when assessing fissure segmentation. The discrepancy rates between our scheme and each of the radiologists are smaller than inter-reader variability and similar to levels reported in previous studies. The preliminary test results demonstrate that our scheme is also reasonably reliable and relatively easy to implement. The geometric representation of the segmented fissures can allow an efficient and robust identification, representation, storage, and visualization of the different geometric lung shapes.

Acknowledgments

This work is supported in part by grants P50 HL084948 and R01 HL085096 from National Heart, Lung, and Blood Institute, National Institutes of Health, to the University of Pittsburgh.

REFERENCES

1. http://www.lungusa.org/site/pp.asp?c=dvLUK9O0E&b=33316.
2. Takahashi1 K, Thompson B, Stanford W, Sato Y, Nagasawa1 K, Sato1 H, Kubota M, Kashiba A, Sugimori H. Visualization of Normal Pulmonary Fissures on Sagittal Multiplanar Reconstruction MDCT. Americal Journal of Roentgenology. 2006; Vol. 187:389–397.
3. Modgil V, Das S, Suri R. Anomalous Lobar Pattern of Right Lung: A Case Report. International Journal of Morphology. 2006; Vol. 24(1):506–507.
4. Venuta F, Rendina EA, Giacomo TD, Flaishman I, Guarino E, Ciccone AM, Ricci C. Technique to Reduce Air leaks after Pulmonary Lobectomy. 1998; Vol. 3(4):361–364.
5. Sluimer I, Schilham A, Prokop M, van Ginneken B. Computer Analysis of Computed Tomography Scans of the Pulmonary: A Survey. IEEE Trans. Medical Imaging. 2006; Vol. 25(4):385–405.
6. Kubo M, Niki N, Eguchi K, Kaneko M, Yamaguchi N. Extraction of Pulmonary Fissures from Thin-Section CT Images by Two-Dimensional Linear Feature Detector Method. Electronics and Communications in Japan (Part II: Electronics). Volume 88(10):59–68.
7. Nakanishi K. Video-Assisted Thoracic Surgery Lobectomy with Bronchoplasty for Lung Cancer: Initial Experience and Techniques. The Annals of Thoracic Surgery. 2007; Vol. 84:191–195. [PubMed: 17588409]
8. Armato SG, Sensakovic WF. Automated Pulmonary Segmentation for Thoracic CT. Academic Radiology. 2004; Vol. 11(9):1011–1021. [PubMed: 15350582]
9. Hu S, Hoffman EA, Reinhardt JM. Automatic Pulmonary Segmentation for Accurate Quantitation of Volumetric X-ray CT Images. IEEE Trans. Medical Imaging. 2001; Vol. 20(6):490–498.

10. Park W, Hoffman EA, Sonka M. Segmentation of Intrathoracic Airway Trees: A Fuzzy Logic Approach. IEEE Trans. Medical Imaging. 1998; Vol. 17(4):489–497.
11. Mori K, Hasegawa J, Suenaga Y, Toriwaki J. Automated Anatomical Labeling of the Bronchial Branch and Its Application to the Virtual Bronchoscopy System. IEEE Trans. Medical Imaging. 2000; Vol. 19(2):103–114.
12. Aylward SR, Bullitt E. Initialization Noise, Singularities, and Scale in Height Ridge Traversal for Tubular Object Centerline Extraction. IEEE Trans. Medical Imaging. 2002; Vol. 21(2):61–75.
13. Aykac D, Hoffman EA, McLennan G, Reinhardt JM. Segmentation and Analysis of the Human Airway Tree from Three-dimensional X-ray CT Images. IEEE Trans. Medical Imaging. 2003; Vol. 22(8):940–950.
14. Pu J, Roos J, A Yi C, Napel S, Rubin GD, Paik DS. Adaptive Border Marching Algorithm: Automatic Lung Segmentation on Chest CT Images. Computerized Medical Imaging and Graphics. 2008; Vol. 32(6):452–462. [PubMed: 18515044]
15. Mullally W, Betke M, Wang J. Segmentation of Nodules on Chest Computed Tomography for Growth Assessment. Medical Physics. 2004; Vol. 31(4):839–848. [PubMed: 15125002]
16. Wang J, Betke M, Ko JP. Pulmonary Fissure Segmentation on CT. Medical Image Analysis. 2006; Vol. 10:530–547. [PubMed: 16807062]
17. Wang, J.; Betke, M.; Ko, JP. Lecture Notes in Computer Science. Vol. Vol. 3216. Berlin, Germany: Springer-Verlag, Medical Image Computing and Computer-Assisted Intervention; 2003. Shape-based Curve Growing Model and Adaptive Regularization for Pulmonary Fissure Segmentation in CT; p. 541-548.
18. Kubo M, Niki N, Nakagawa S, Eguchi K, Kaneko M, Moriyama N, Omatsu H, Kakinuma R, Yamaguchi N. Extraction Algorithm of Pulmonary Fissures from Thin-section CT Images Based on Linear Feature Detector Method. IEEE Trans. Nuclear Science. 1999; Vol. 46(6):2128–2133.
19. Kubo, M.; Kawata, Y.; Niki, N.; Eguchi, K.; Ohmatsu, H.; Kakinuma, R.; Kaneko, M.; Kusumoto, M.; Moriyama, N.; Mori, K.; Nishiyama, H. Automatic Extraction of Pulmonary Fissures from Multidetector-row CT Images. Proceedings of the IEEE International Conference on Image Processing (ICIP'01); Greece. 2001. p. 1091-1094.
20. Kuhnigk, JM.; Hahn, H.; Hindennach, M.; Dicken, V.; Krass, S.; Peitgen, HO. Pulmonary Lobe Segmentation by Anatomy-guided Three-dimensional Watershed Transform; Proceedings of SPIE (Medical Imaging); 2003. p. 1482-1490.
21. Zhou, X.; Hayashi, T.; Hara, T.; Fujita, H.; Yokoyama, R.; Kiryu, T.; Hoshi, H. Automatic Recognition of Pulmonary Lobes and Fissures from Multi-slice CT Images; Proceeding of SPIE (Medical Imaging); 2004. p. 1629-1633.
22. Saita S, Kubo M, Kawata Y, Niki N, Ohmatsu H, Moriyama N. An Algorithm for the Extraction of Pulmonary Fissures from Low-dose Multislice CT Image. System and Computers in Japan. 2006; Vol. 37(9):63–76.
23. Zhang, L.; Hoffman, EA.; Reinhardt, JM. Pulmonary Lobe Segmentation by Graph Search with 3-D Shape Constraints; Proceedings of SPIE (Medical Imaging); 2001. p. 204-215.
24. Zhang, L.; Reinhardt, JM. Detection of Pulmonary Lobar Fissures using Fuzzy Logic; Proceedings of SPIE (Medical Imaging); 1999. p. 188-199.
25. Zhang L, Hoffman EA, Reinhardt JM. Atlas-driven Pulmonary Lobe Segmentation in Volumetric X-ray CT Images. IEEE Trans. Medical Imaging. 2006; Vol. 25(1):1–16.
26. van Rikxoort EM, van Ginneken B, Klik M, Prokop M. Supervised Enhancement Filters: Application to Fissure Detection in Chest CT Scans. IEEE Trans. Medical Imaging. 2008; Vol. 27(1):1–10.
27. Hayashi K, Aziz A, Ashizawa K, Hayashi H, Nagaoki K, Otsuji H. Radiographic and CT Appearances of the Major Fissures. Radiographics. 2001; Vol. 21(4):861–874. [PubMed: 11452059]
28. Pu J, Zheng B, Leader JK, Wang XH, Gur D. An Automated CT Based Lung Nodule Detection Scheme Using Geometric Analysis of Signed Distance Field. Medical Physics. 2008; Vol. 35(8): 3453–3461. [PubMed: 18777905]

29. Pu J, Roos J, CA Yi, Napel S, Rubin GD GD, Paik DS. Adaptive Border Marching Algorithm: Automatic Lung Segmentation on Chest CT Images. Computerized Medical Imaging and Graphics. 2008; Vol. 32(6):452–462. [PubMed: 18515044]
30. Brown MS, McNitt-Gray MF, Goldin JG, Suh RD, Sayre JW, Aberle DR. Patient-Specific Models for Lung Nodule Detection and Surveillance in CT Images. IEEE Trans. Medical Imaging. 2001; Vol. 20(12):1242–1250.
31. Li Q, Katsuragawa S, Doi K. Computer Aided Diagnostic Scheme for Lung Nodule Detection in Digital Chest Radiographs by Use of a Multiple-Template Matching Technique. Medical Physics. 2001; Vol. 28(10):2070–2076. [PubMed: 11695768]
32. Armato SG III, Giger MI, Moran CJ, Blackburn JT, Doi K, MacMabon H. Computerized Detection of Pulmonary Nodules on CT Scans. Radiographics. 1999; Vol. 19:1303–1311. [PubMed: 10489181]
33. Lorensen WE, Cline HE. Marching Cubes: A High Resolution Three-dimensional Surface Construction Algorithm. Computer Graphics. 1987; Vol. 21(4):163–169.
34. Field DA. Laplacian Smoothing and Delaunay Triangulations. Communications in Applied Numerical Methods. 1988; Vol. 4:709–712.
35. Vollmer J, Mencl R, Müller H. Improved Laplacian Smoothing of Noisy Surface Meshes. Computer Graphics Forum. 1999; Vol. 18(3):131–138.
36. Ohtake, Y.; Belyaev, AG.; Bogaevski, IA. Polyhedral Surface Smoothing with Simultaneous Mesh Regularization. Proceedings of the Geometric Modeling and Processing; Hong Kong (China). 2000. p. 229-237.
37. Horn, B. Extended Gaussian Images. Proc. IEEE 72; New Orleans, USA. 1984. p. 1671-1686.
38. Venuta F, Rendina EA, Giacomo TD, Flaishman I, Guarino E, Ciccone AM, Ricci C. Technique to Reduce Air Leaks after Pulmonary Lobectomy. European Journal of Cardio-Thoracic Surgery. 1998; Vol. 13(4):361–364. [PubMed: 9641332]
39. Chalana V, Kim Y. A Methodology for Evaluation of Boundary Detection Algorithms on Medical Images. IEEE Trans. Medical Imaging. 1997; Vol. 16(5):642–652.
40. Zhang YJ. A Survey on Evaluation Methods for Image Segmentation. Pattern Recognition. 1996; Vol. 29:1335–1346.
41. Ohtake Y, Belyaev A, Seidel HP. Ridge-Valley Lines on Meshes via Implicit Surface Fitting. ACM Trans. Graphics (SIGGRAPH'2004). 2004; Vol. 23(3):609–612.
42. Pu J, Ramani K. On Visual Similarity Based 2D Drawing Retrieval. Computer Aided Design. 2006; Vol. 38(3):249–259.
43. Osada R, Funkhouser T, Chazelle B, Dobkin D. Shape Distribution. ACM Trans. Graphics. 2002; Vol. 21(4):807–832.

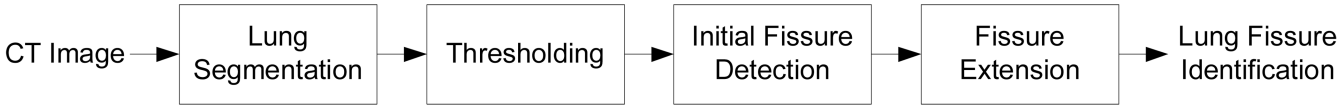

Fig. 1.
Schematic diagram of the lung fissure detection algorithm.

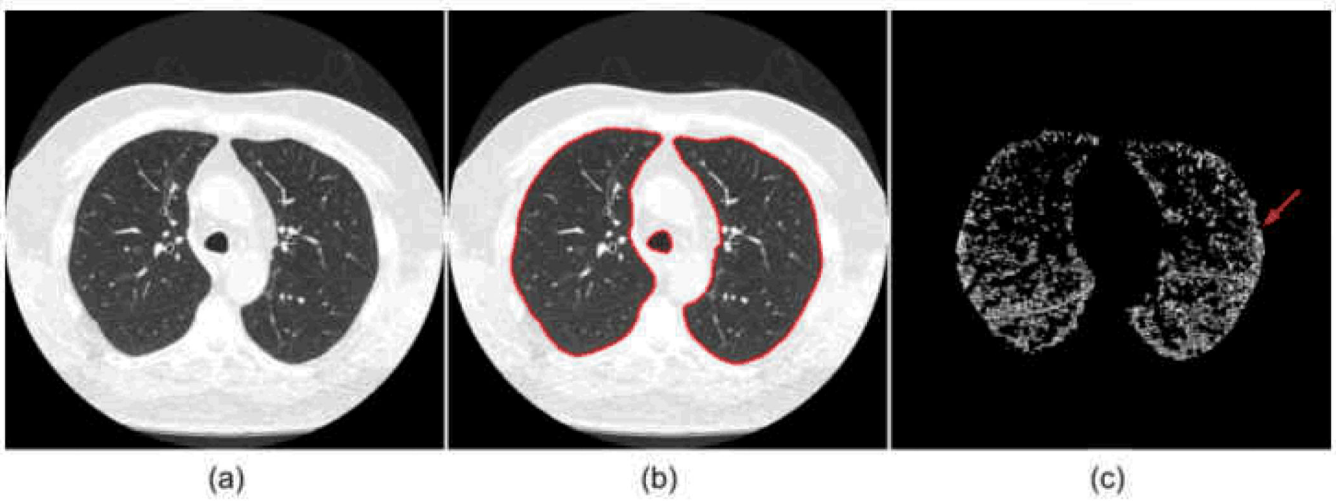

Fig 2.

(a) Original CT image. (b) Segmented lung region (red contour). (c) Lung region after application of the threshold band (i.e., −800 to −400 HU). The arrow in (c) indicates a point on lung boundary that is used in a later example.

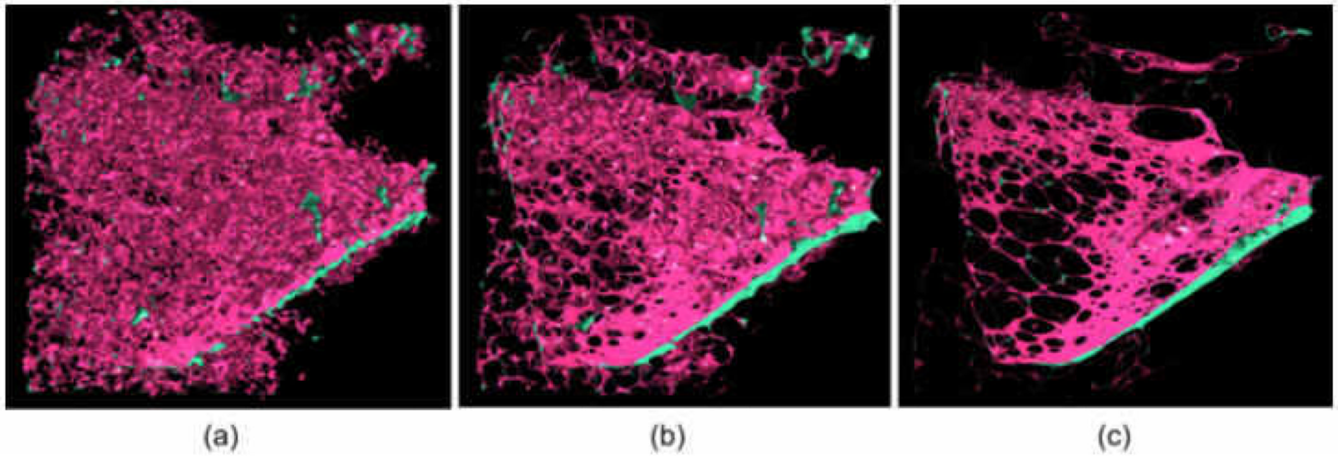

Fig. 3.

A 50×50×50 mm^3 sub-volume extracted from a CT scan and modeled using the MCA with a threshold of −800 HU (a) and filtered results using Laplacian smoothing operation repeated 10 times (b) and repeated 20 times (c).

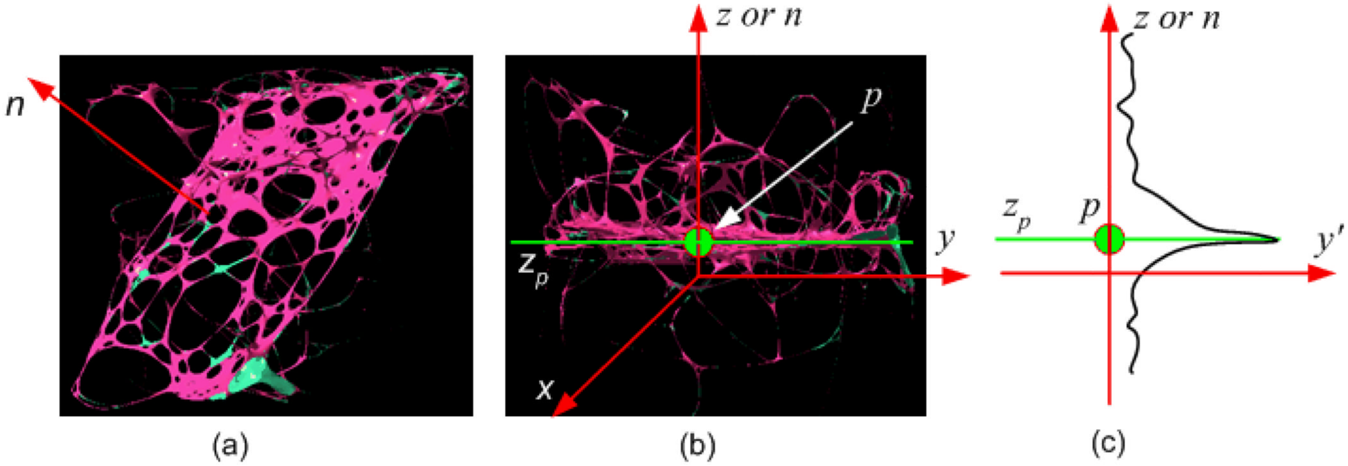

Fig. 4.

Steps in the fissure extraction process: (a) determining the normal vector *n* of the fissure using EGI; (b) transforming (or rotating) the fissure and aligning the normal vector *n* with the z-axis that is perpendicular to the CT image; and (c) constructing the histogram by projecting the z-values of all points in the fissure model onto the z-axis, where z_p is the plane on which the fissure is located at a point with the maximum value of the histogram (i.e., z = *p*).

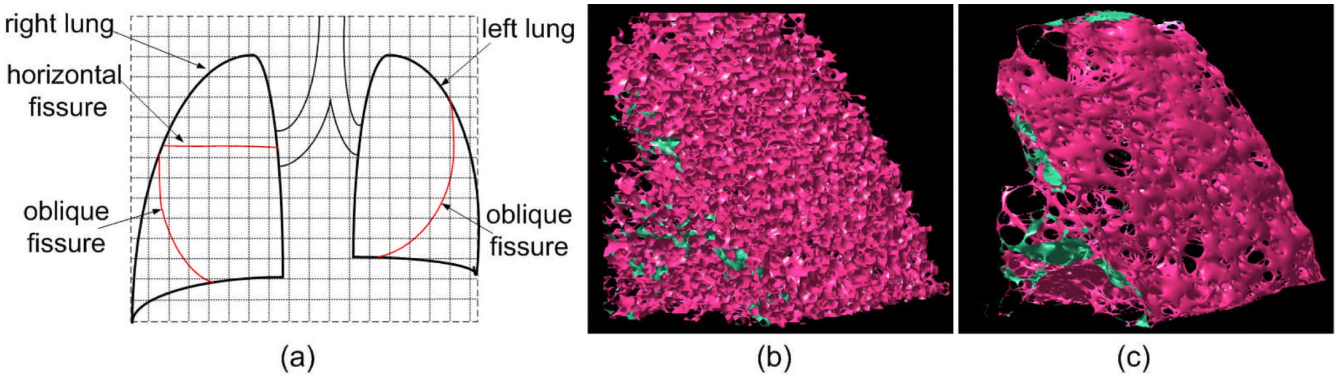

Fig. 5.
Illustration of a volumetric grid system applied to a CT examination: (a) the bounding box of the lung volume is divided into a three-dimensional grid system. Each vertex of a cell acts as a center of a sub-volume for EGI-based fissure detection; (b) the modeled result of a sub-volume with a size of 15×15×15 mm^3 centered at the lung boundary as indicated by the arrow in Fig. 2(c); and (c) the geometric model after the Laplacian smoothing operation is applied to the model in (b) for 20 times.

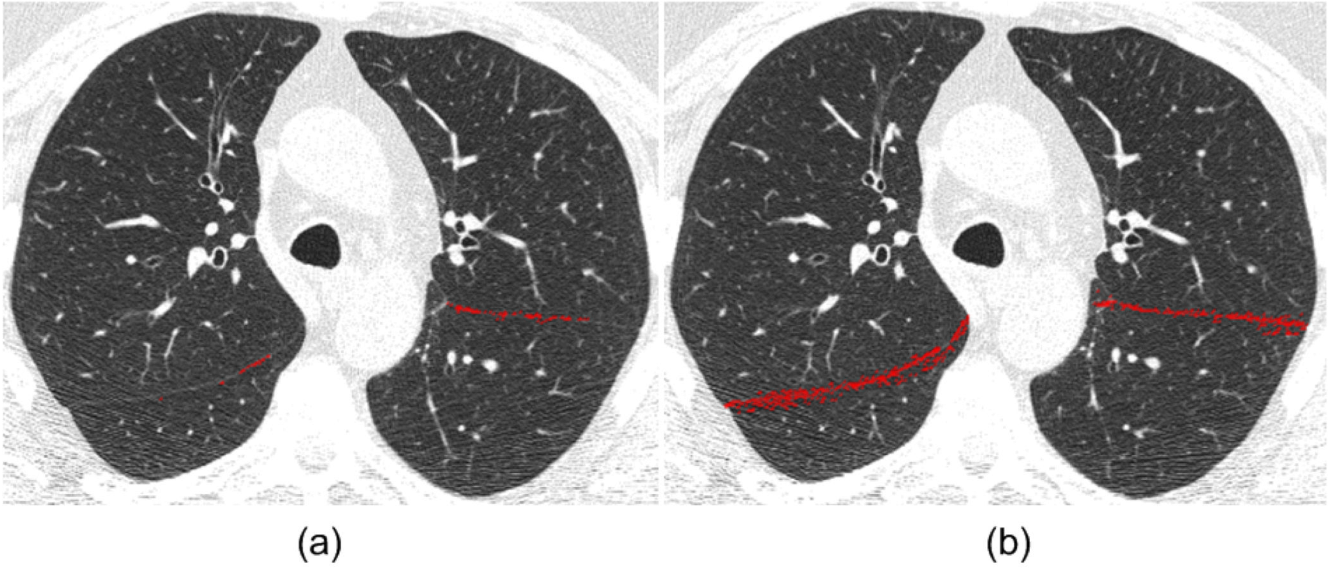

Fig. 6.
An example of the initial fissure detection (a) and the final fissure extension (b).

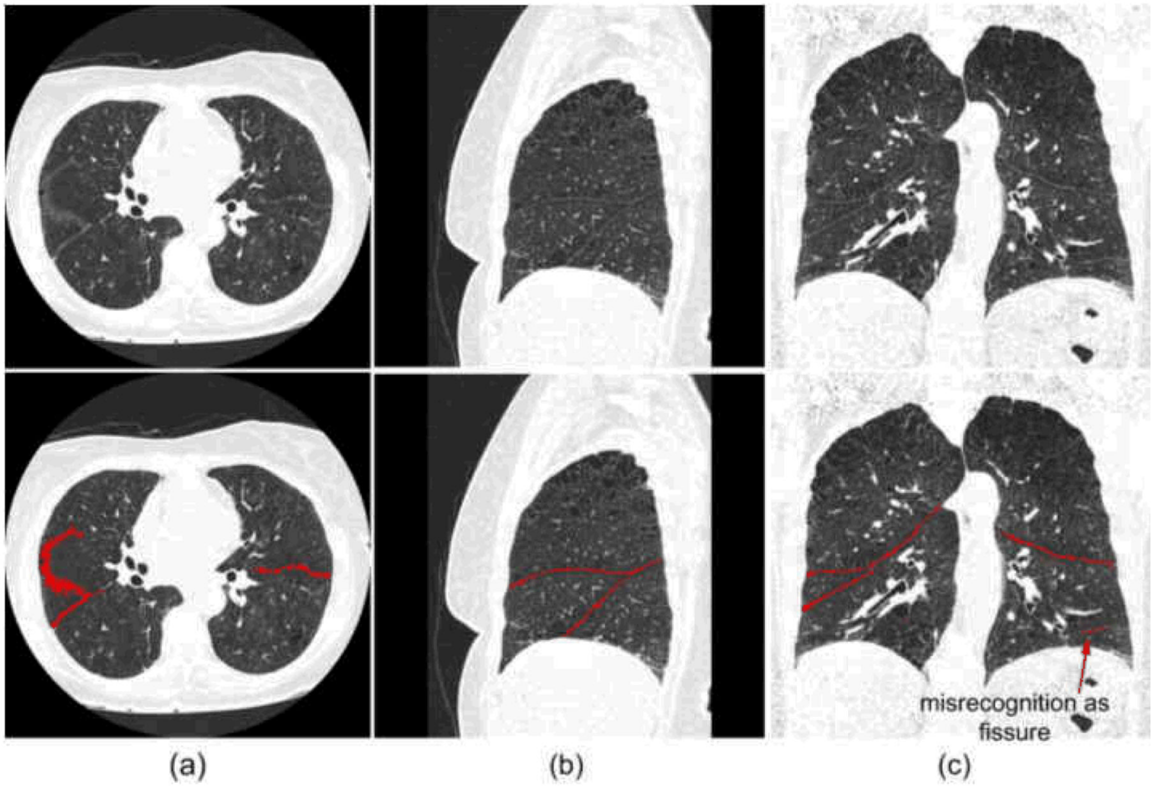

Fig. 7.

Examples of automated fissure detection results in an axial view (a), coronal view (b), and sagittal view (c). The top row shows the original images and the bottom row shows images with overlay of the automated detection results.

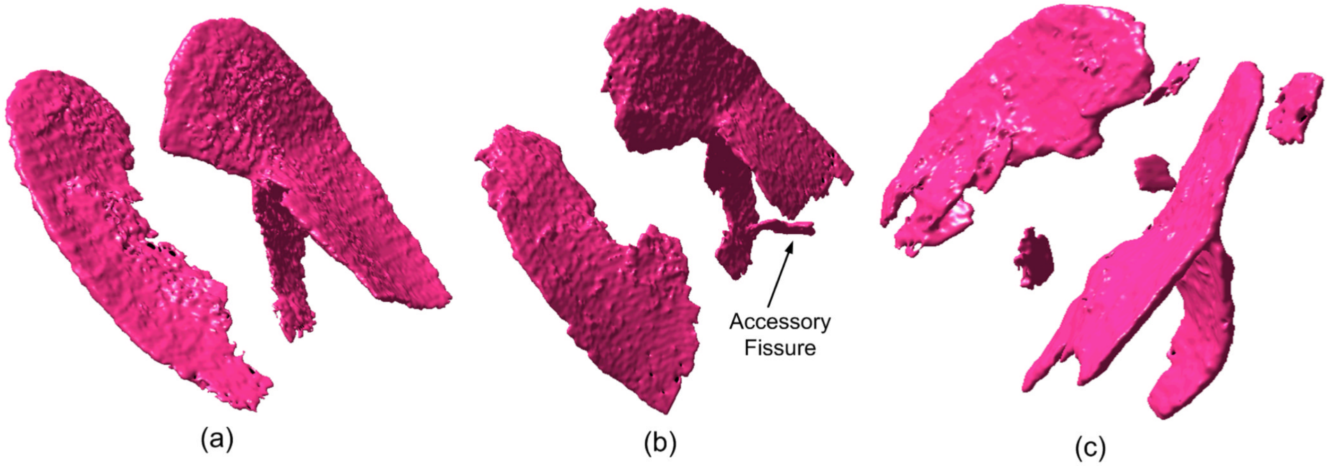

Fig. 8.
Illustration of detected fissures in three sets of CT examinations: (a) the fissures detected in the examination shown in Fig 2; (b) an example in which an accessory fissure was detected; and (c) an example where a number of non-fissure regions were detected because they are represented by a plane-like shape.

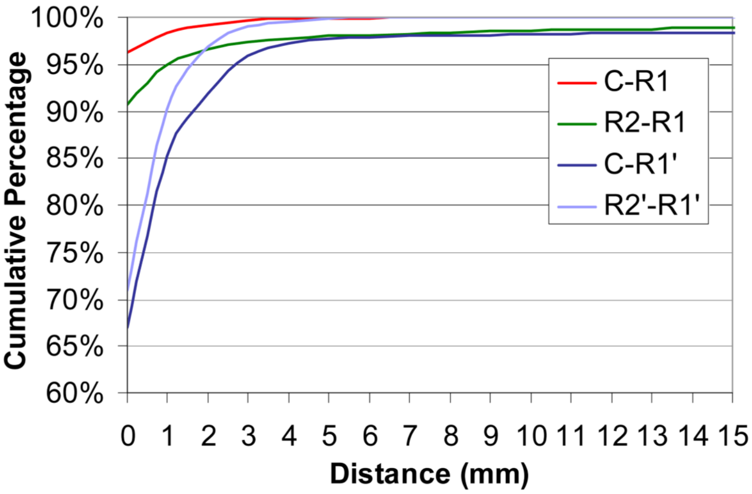
100%
95%
90%
85%
80%
75%
70%
65%
60%
Cumulative Percentage
0
1
2
3
4
5
6
7
8
9
10
11
12
13
14
15
Distance (mm)
C-R1
R2-R1
C-R1'
R2'-R1'

(a)

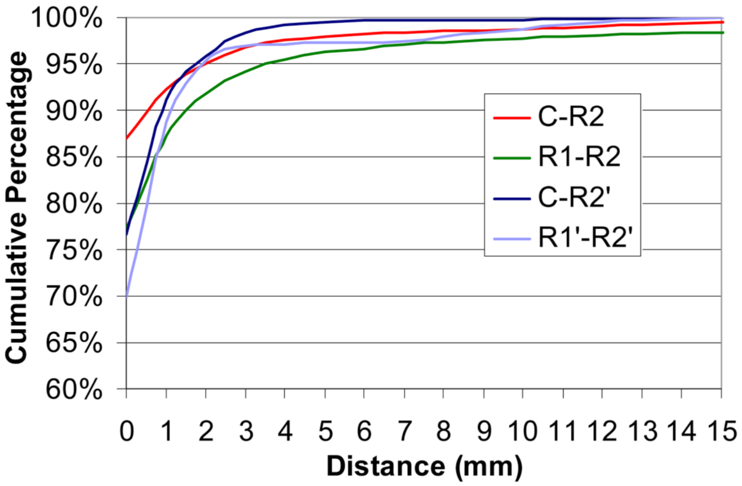

(b)

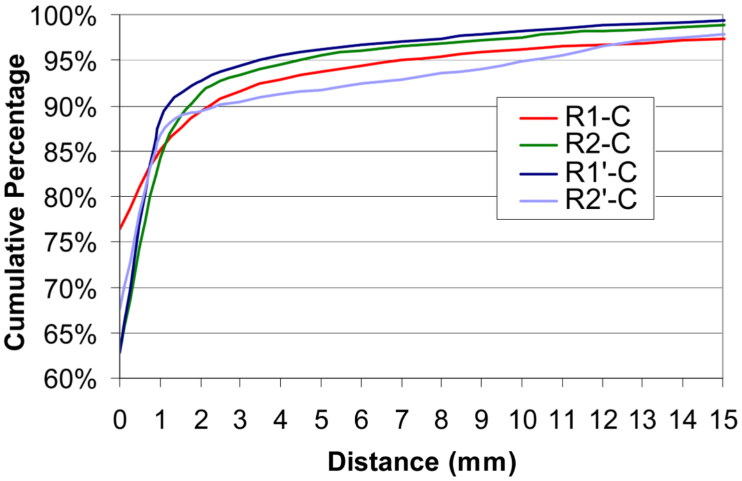

(c)

Fig. 9.

Three sets (family) of curves show the cumulative error distance distributions (CEDD): (a) the results marked by radiologist #1 are used as the reference; (b) the results marked by radiologist #2 are used as the reference; and (c) the scheme-segmented results are used as the reference. In these curves “C” denotes the scheme-segmented results, “R1” and “R2” denote the fissures as marked by either radiologist when “guided” by the automated segmentation results, and “R1´” and “R2´” denote the fissures as marked by either radiologist without viewing computerized results.

Table 1

Summary of fissure segmentation performance for the 10 cases as measured by Root-Mean-Square (RMS) distances (mm) and the associated overall standard deviations (mm).

Case No.	C-R1	C-R2	R1-C	R2-C	R2-R1	R1-R2
1	0.177	1.724	1.234	0.465	0.352	2.190
2	0.193	0.280	2.895	0.757	0.484	2.706
3	0.208	2.833	0.780	0.681	0.329	2.809
4	0.152	0.455	1.361	0.518	0.293	0.623
5	0.149	1.190	1.530	1.208	0.570	1.043
6	0.057	1.227	0.589	1.049	0.851	1.985
7	7.237	0.660	0.834	1.198	7.307	0.749
8	0.655	0.621	1.221	7.505	7.541	0.888
9	11.114	10.093	1.014	0.725	14.890	9.981
10	0.418	0.527	3.345	0.899	0.736	3.390
Average	2.04±3.8	1.96±2.96	1.48±0.92	1.48±2.13	3.34±4.98	2.64±2.76

Table 2

Percent agreement between our computerized scheme (CAD) and each of the two radiologists (R1 and R2) as a function of predetermined distances.

	Experiment One (100 CT images)		**Experiment Two (10 CT images)**	
	distance ≤ 2 mm	**distance ≥ 3 mm**	**distance ≤ 2 mm**	**distance ≥ 3 mm**
CAD→ R1	98.7	0.9	91.9	4.1
CAD → R2	94.9	3.5	95.9	1.6
R1 → CAD	89.4	8.4	91.4	6.6
R2 → CAD	90.1	7.4	88.6	9.1
R1 → R2	91.8	5.9	95.3	3.1
R2 → R1	96.7	2.7	96.9	1.2